Strain-driven structure-ferroelectricity relationship in hexagonal TbMnO3 films

R. Mandal, M. Hirsbrunner, V. Roddatis, R. Gruhl, L. Schüler, U. Roß, S. Merten, Philipp Gegenwart, V. Moshnyaga

Angaben zur Veröffentlichung / Publication details:

Mandal, R., M. Hirsbrunner, V. Roddatis, R. Gruhl, L. Schüler, U. Roß, S. Merten, Philipp Gegenwart, and V. Moshnyaga. 2020. "Strain-driven structure-ferroelectricity relationship in hexagonal TbMnO3 films." *Physical Review B* 102 (10): 104106. https://doi.org/10.1103/physrevb.102.104106.

PHYSICAL REVIEW B **102**, 104106 (2020)

Strain-driven structure-ferroelectricity relationship in hexagonal TbMnO$_3$ films

R. Mandal,[1,2] M. Hirsbrunner,[1] V. Roddatis,[3] R. Gruhl,[4] L. Schüler,[1] U. Roß,[3] S. Merten,[1]
P. Gegenwart,[4] and V. Moshnyaga[1,*]
[1]*Erstes Physikalisches Institut, Georg-August-Universität Göttingen, Friedrich-Hund-Platz 1, 37077 Göttingen, Germany*
[2]*Department of Physics, Indian Institute of Science Education and Research, Pune 411008, India*
[3]*Institut für Materialphysik, Georg-August-Universität Göttingen, Friedrich-Hund-Platz 1, 37077 Göttingen, Germany*
[4]*Experimentalphysik VI, Center for Electronic Correlations and Magnetism,*
Augsburg University, D-86159 Augsburg, Germany

(Received 2 June 2020; revised 19 August 2020; accepted 2 September 2020; published 18 September 2020)

Thin films and heterostructures of hexagonal manganites as promising multiferroic materials have attracted a considerable interest. We report structural transformations of high-quality strain-stabilized epitaxial hexagonal TbMnO$_3$/yttria stabilized zirconia(111) (h-TMO) films, analyzed by means of various characterization techniques. A reversible structural phase transition from $P6_3cm$ to $P6_3/mmc$ structure at $T_C \sim 800\,\mathrm{K}$ was observed in stoichiometric h-TMO films by temperature-dependent Raman spectroscopy and optical ellipsometry. The latter, directly probing the electronic system, indicates its modification at the structural phase transition, likely due to charge transfer from oxygen to Mn. A partially reversible phase transformation and stress relaxation was observed in h-TMO films with Tb excess after temperature cycling (300-1000-300 K) during Raman and ellipsometry. An inhomogeneous microstructure, containing ferroelectric and paraelectric nanodomains, was revealed by transmission electron microscopy in the Tb-rich film after annealing. The results obtained indicate a strong influence of stress, induced by temperature and by constrained sample geometry, onto the structure and ferroelectricity of strain-stabilized h-TMO thin films.

DOI: 10.1103/PhysRevB.102.104106

I. INTRODUCTION

Rare-earth manganites, REMnO$_3$ with RE = La to Lu, manifest a family of strongly correlated electronic oxides with rich emerging properties, like high-temperature ferroelectricity, magnetic ordering, and magnetoelectric coupling [1,2]. Two distinct crystal structures, i.e., orthorhombic ($Pnma$) and hexagonal ($P6_3cm$), were revealed for large (La, Pr, Nd, Sm, Gd, Tb, Dy) and small (Y, Ho, Er, Tm, Yb, Lu) RE cations, respectively. In the $Pnma$ structure, the improper ferroelectricity with very low Curie temperatures, $T_C \sim 15\,\mathrm{K}$ (o-HoMnO$_3$) [3], has a magnetoelastic origin; the modulation of magnetic structure results in a typically small spontaneous polarization, $P_s = 0.5\,\mu\mathrm{C/cm^2}$ (GdMnO$_3$) [4]. In contrast, the ferroelectricity in the hexagonal phase originates from the geometric distortion yielding a very high $T_C \sim 1000\,\mathrm{K}$ [5,6] and much larger polarization, e.g., $P_s = 5.5\,\mu\mathrm{C/cm^2}$ in h-YMnO$_3$ [7,8]. For hexagonal manganites ferroelectricity arises from the K_3 tilting of the MnO$_5$ bipyramids. The coupling of this distortion to the polar Γ_2^- mode along with a buckling of RE layer [9] results in an off-centrosymmetric displacement of oxygen and rare-earth atoms. These structural modifications, having the form of buckling of atomic chains [10], can be directly visualized by means of high-resolution electron microscopy.

Especially interesting for nanoscale science and applications could be epitaxial h-REMnO$_3$ films and heterostructures, the growth of which was already demonstrated by different physical and chemical vapor deposition techniques [11]. There were published several reports [6,12–14] on hexagonal films with small RE cations (Ho, Er, Y), showing relatively high ferroelectric transition temperatures, e.g., $T_C = 875$–$1100\,\mathrm{K}$ and large saturation polarization, $P_S \sim 10$–$12\,\mu\mathrm{C/cm^2}$. However, the h-YMnO$_3$ thin films possess a lower polarization ($1.7\,\mu\mathrm{C/cm^2}$) than its bulk form ($5.5\,\mu\mathrm{C/cm^2}$) [15]. General features of thin films, pointed out by Fontcuberta [15], are the reduced values of remnant polarization and ferroelectric Curie temperatures compared to the bulk values. In addition, nanodomains with orientations different from the main epitaxial phase were observed for films with different thickness and grown by different techniques [16]. Likely, such nanodomains are responsible for the reduction of the remnant polarization. Another important parameter, strongly influencing the properties of thin h-REMnO$_3$ films, is the partial pressure of oxygen, pO$_2$, during preparation and related to it oxygen deficiency. Jang *et al.* [12] related the oxygen deficiency to be responsible for the appearance of magnetic disorder and spin-glass state concurring with the dominating antiferromagnetic ordering in h-REMnO$_3$ films. Moreover, the development of an inhomogeneous stress state and strain gradient in the HoMnO$_3$ films, prepared at pO$_2$ ~ 10–300 mbar, is shown to be influenced by oxygen deficiency, resulting in a giant flexoelectric effect [6] for films grown at low pO$_2$.

---

[*] vmosnea@gwdg.de

2469-9950/2020/102(10)/104106(10)

Much less is, however, known on the h-REMnO$_3$ films with larger RE cation, like Tb, which can be obtained as a metastable phase in strain-stabilized thin films. The reports on the preparation of hexagonal TbMnO$_3$/Yttria Stabilized Zirconia(111) (h-TbMnO$_3$) films are scarce and the obtained results are controversial. Namely, Lee *et al.* [17,18] demonstrated a stabilization of the hexagonal phase in TMO films grown by means of pulsed laser deposition (PLD) on Pt(111)/Al$_2$O$_3$(0001) and yttrium-stabilized zirconia [YSZ(111)] substrates. The films were found to be ferroelectric (FE) with $T_C \sim 60$ K and a transition into an antiferroelectric (AFE) phase for $T > T_C$ was observed. Kim *et al.* [19] reported ferroelectricity at room temperature in a PLD-grown h-TMO film and demonstrated the switching of the ferroelectric polarization by means of a piezo-force microscopy; no AFE phase was observed in contradiction with the previous report. By first-principle calculations Kim *et al.* [19] predicted the ferroelectricity in h-TMO to have the same mechanism as in other hexagonal manganites. However, the information on the ferroelectric domain structure as well as on the Curie temperature for this strain-stabilized h-TMO phase is still absent and the microscopic origin of this FE phase was not experimentally confirmed. A special interest for the h-TMO films is motivated by its lower thermodynamic stability, compared to other h-manganites (R = Y–Lu), which allows one to expect a pronounced influence of the lattice strain on the ferroelectric/structural phase transition.

The high-temperature structural/ferroelectric transitions in h-manganites have been studied by x-ray diffraction (XRD) [20]. A one-step transition from the low-temperature $P6_3cm$ structure to the high-temperature $P6_3/mmc$ structure was shown, primarily caused by the RE-O$_P$ displacement of the K_3 phonon mode. A nonlinear optical second-harmonic generation (SHG) as a contact-free technique [5,21–23], probing the spontaneous polarization, allows one to determine the ferroelectric T_C. However, as noted in Ref. [5] to avoid the inhomogeneity effects due to differently polarized ferroelectric domains, a preparation of single-domain state by poling and, hence, the availability of a bottom electrode is necessary even for SHG study of a thin film. In addition, Raman scattering was also shown to be an effective nondestructive optical probe of the structural phase transition in hexagonal manganites. Applied to YMnO$_3$ bulk samples it reveals the change of the A_1 symmetry of the dominating phonon mode at $\sim 680\,\mathrm{cm}^{-1}$ in the ferroelectric $P6_3cm$ into the A_{1g} symmetry in the paraelectric $P6_3/mmc$ phase [24]. However, studies of high-temperature phase transitions in h films are very limited—one can mention the observation of ferroelectric $T_C \sim 1020$ K by monitoring the temperature behavior of the A_1 mode in the Raman spectra of the multiferroic 200-nm-thick h-LuFeO$_3$ thin film [25].

One can conclude that although the ferroelectric behavior of the h-RMnO$_3$ films was well documented, their ferroelectric (T_C) and magnetic (T_N) values, as a rule, were found to be smaller than those obtained in the corresponding bulk materials. The deviations of the film properties were assigned to the formation of oxygen vacancies [12] as well as to the epitaxy strain [26] and strain gradient effects [6]. Here we report h-TMO/YSZ(111) films grown by means of a metalorganic aerosol deposition (MAD) technique [27], which provides a high partial oxygen pressure pO$_2$ ~ 0.2 bar during deposition, allowing prevention of the formation of oxygen vacancies in the film. In addition, the close to equilibrium MAD growth conditions result in epitaxial coherently grown TMO films on YSZ(111) with perfect crystallinity as well as atomically sharp and flat film/substrate interfaces. The atomically resolved High-angle annular dark-field – scanning transmission electron microscopy (HAADF-STEM) evidences the characteristic periodic buckling of Tb ions, indicating the presence of the FE domains, vertically aligned with respect to the film plane. The FE/Paraelectric (PE) transition at $T_C \sim 800$ K was determined by means of temperature-dependent Raman spectroscopy and optical ellipsometry.

II. EXPERIMENTS

The h-TMO films with a thickness $d = 50$ nm have been grown by means of MAD technique [27] on commercial YSZ(111) substrates (Crystal GmbH) by using Tb- and Mn-acetylacetonates as precursors. Precursor solutions in dimethylformamide with concentration 0.02 M for Mn precursor and molar ratios Tb/Mn = 1.15 and 1.2 were used. The films were grown with the rate, $v = 6\,\mathrm{nm/min}$, by spraying the precursor solution by using dried compressed air onto the YSZ substrate heated to $T_{\mathrm{sub}} \sim 900$-$1000\,^\circ\mathrm{C}$ in ambient atmosphere. After preparation the films were quenched in 1 min down to 600 °C and then cooled in 10 min down to room temperature. The substrate temperature was controlled by a pyrometer and by *in situ* optical ellipsometry.

XRD (Cu-K$_\alpha$ radiation, Θ-2Θ Bragg–Brentano geometry), rocking curves (ω scans), asymmetric ϕ scan, reciprocal space mapping, and small-angle x-ray reflectivity were used to characterize the structure and the thickness of the films. Polarization-dependent Raman spectroscopy was carried out at room temperature by using a confocal Raman microscope (LabRAM HR Evolution, HORIBA Jobin Yvon) in a back-scattering geometry with a radiation of He-Ne laser ($\lambda = 632.8\,\mathrm{nm}$, $P_0 = 1.3\,\mathrm{mW}$). Temperature-dependent Raman measurements were performed in a back-scattering geometry with a long-range 50× objective on the film samples, glued by Ag paste on a Cu sample holder, mechanically attached to a TiN resistive heater. A NiCr-Ni thermocouple was used to measure the temperature of the Cu sample holder.

The *in situ* optical ellipsometry was measured during the growth, cooling, and subsequent heating of the films by using a home-made optical setup [27] of the polarizer-modulator-sample-analyzer type [28]. A He-Ne laser beam ($\lambda = 632.8\,\mathrm{nm}$) was focused on the sample at an incident angle close to the Brewster angle of YSZ substrate, $\theta_B \sim 60.5^\circ$. The ellipsometric phase-shift angle, Δ, and polarization rotation angle, Ψ, were measured by using lock-in technique at fundamental and second-harmonic frequencies, $\omega = 50\,\mathrm{kHz}$ and 2ω, respectively (ω is the modulation frequency of the light polarization). The real and imaginary part of refraction index at $\lambda = 632.8\,\mathrm{nm}$ was calculated using Fresnel formulas by modeling the sample as a thin film and infinitely thick YSZ substrate (see Supplemental Material (SM) as Ref. [29]).

The local structure of TMO films was studied by scanning transmission electron microscopy (STEM) using an FEI Titan 80–300 G2 environmental transmission electron microscope,

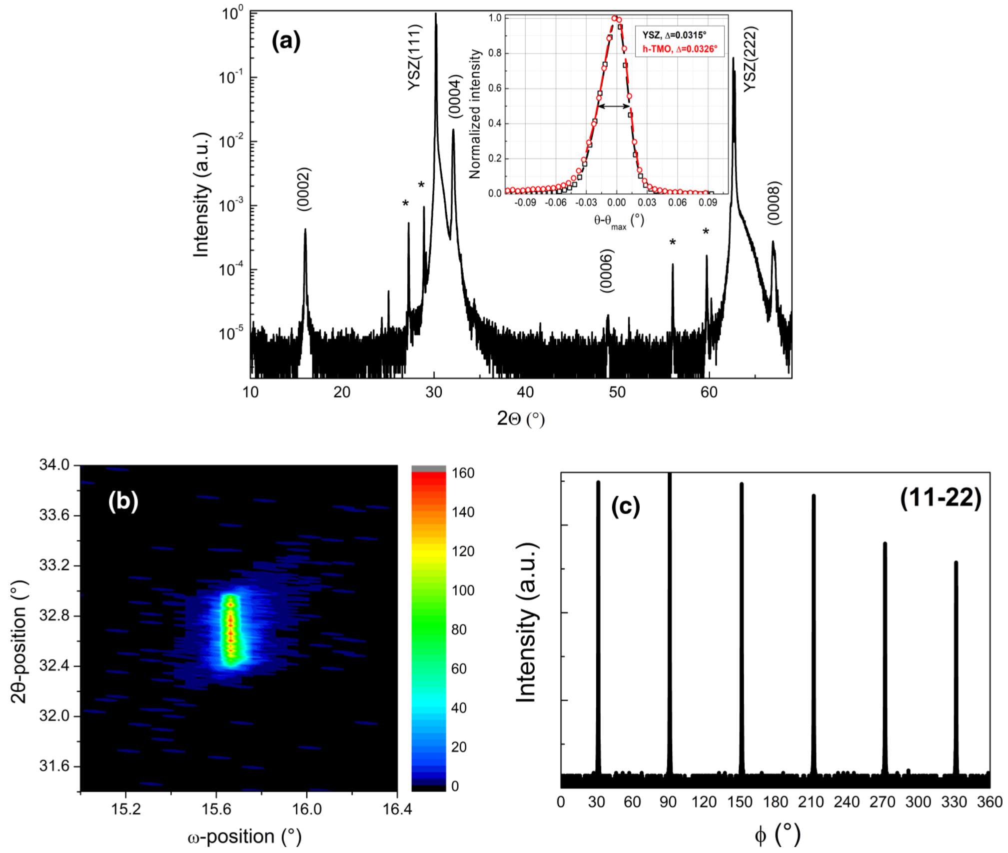

FIG. 1. Structural characterization of h-TMO/YSZ(111) films: (a) XRD (Θ-2Θ) pattern of a representative film shows the (000*l*) out-of-plane epitaxy. The inset demonstrates rocking curves of h-TMO(0002) and YSZ(111) peaks with almost the same FWHM~0.032°; (b) Reciprocal-space mapping of a film (11-22) peak and c) a phis can of the (11-22) film peak evidences the in-plane epitaxy with hexagonal symmetry.

operated at an acceleration voltage of 300 kV. TEM lamellas were prepared by focused ion-beam lift-out technique using a ThermoFisher (formerly FEI) Helios 4UC instrument.

III. RESULTS AND DISCUSSION

In Fig. 1(a) we show the XRD patterns of a stoichiometric TMO/YSZ(111) film, prepared with an optimal precursor molar ratio Tb/Mn = 1.15. Along with the YSZ(111) substrate peaks one can see the system of reflexes from the (000*l*) planes of a h-TMO phase, evidencing an out-of-plane epitaxial growth. The calculated *c*-axis lattice parameter $c = 1.1182\,\mathrm{nm}$ is, from one side, significantly smaller than the theoretically estimated value $c_0 = 1.153\,\mathrm{nm}$ for a strain-free h-TMO film [19] and, from another side, is much closer to the theoretical value for a strained h-TMO film, $c_{\mathrm{th}} = 1.1057\,\mathrm{nm}$, also obtained by first-principles calculations [19]. Comparing the measured and the theoretical values of the *c*-lattice parameter for strain-free h-TMO, a large out-of-plane tensile stress, $\varepsilon_\perp = (c - c_0)/c_0 \approx -3\%$, can be deduced in the MAD-grown h-TMO/YSZ films. Note that the theoretically estimated value of the in-plane *a*-lattice constant for a strain-free h-TMO is $a_0 = 0.620\,\mathrm{nm}$ [19], but one cannot compare it with the bulk strain-free value simply because TMO does not exist in the bulk form. However, considering the in-plane epitaxy relation $[11\text{-}20]_{\mathrm{TMO}} \parallel [110]_{\mathrm{YSZ}}$ [30,31] observed for epitaxial growth of h-$YMnO_3$/YSZ(111) films, the corresponding in-plane film/substrate lattice mismatch $(\sqrt{2}a_{\mathrm{TMO}}/\sqrt{3}a_{\mathrm{YSZ}} - 1)$ would be fully compensated for a hypothetical TMO film with in-plane lattice constant, $a_{\mathrm{TMO}} = (\sqrt{3}/\sqrt{2})a_{\mathrm{YSZ}} = 0.6277\,\mathrm{nm}$ $(a_{\mathrm{YSZ}} = 0.5125\,\mathrm{nm}$ [32]). We performed the reciprocal-space mapping of the TMO(11-22) peak [see Fig. 1(b)] and, considering the measured *c*-axis lattice parameter, $c = 1.1182\,\mathrm{nm}$, the in-plane lattice constant $a = 0.6277\,\mathrm{nm}$ of h-TMO/YSZ(111) film was determined. The measured value fits perfectly to the above estimated hypothetical a_{TMO}, thus evidencing a full compensation of the film/substrate in-plane misfit. It exceeds the theoretically estimated lattice constant of a strained-free h-TMO, $a_0 = 0.620\,\mathrm{nm}$ [22] and implies the presence of an in-plane stress $\varepsilon_\parallel = (a_0 – a_{\mathrm{TMO}})/a_0 = -1.2\%$ in the h-TMO/YSZ(111) film.

Importantly, no signs of the orthorhombic phase or other impurity phases were seen in XRD for the MAD-grown h-TMO films. The rocking curve of the (0002) peak, shown in the inset of Fig. 1(a), displays a full width at half maximum, $\mathrm{FWHM}_{\mathrm{TMO}} = 0.033°$, which is very close to that for the substrate, $\mathrm{FWHM}_{\mathrm{YSZ}} = 0.032°$, measured with our XRD setup. Thus, the crystalline quality of our h-TMO/YSZ(111) films is solely determined by the substrate quality as should be in the case of a true epitaxial growth. In-plane epitaxy of a h-TMO film was verified by the full ϕ scan around the (11-22) peak shown in Fig. 1(c). It obeys a sixfold hexagonal symmetry

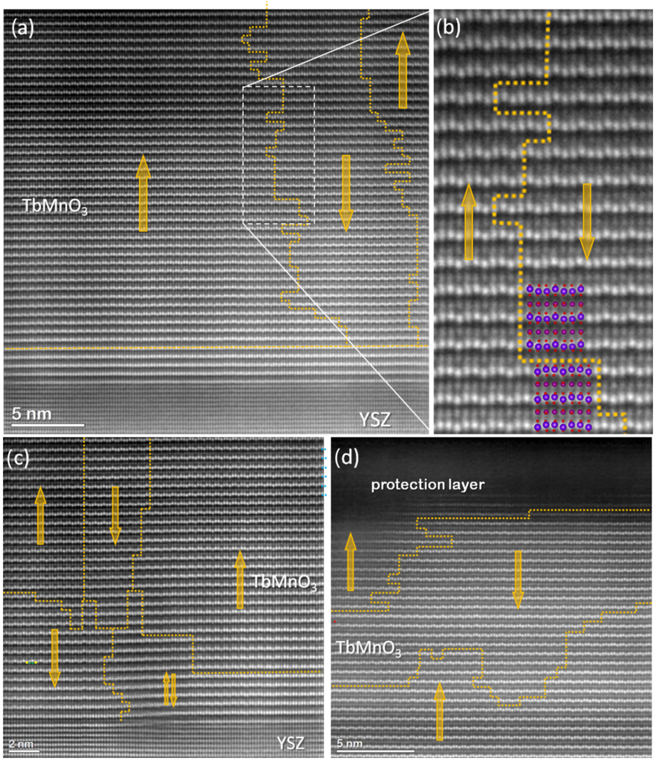

FIG. 2. (a) High resolution cross-section TEM image of a h-TMO/YSZ(111) film measured along the [11-20] crystallographic direction of the film with characteristic buckling (rumpling) of Tb atoms. The arrows show the direction of the ferroelectric polarization within one domain. Atomically smooth and flat film/substrate interface as well as the absence of Tb rumpling can be seen in the very first 4 u.c. of the film. (b) Zoomed part of (a) demonstrates the characteristic regions with the up- (left part) and down rumpling (right part) of Tb ions, separating FE domains with a typical size varying in the range 5–20 nm. (c) HR-STEM image of TbMnO$_3$/YSZ interface showing the origin of FE domain at the atomic height step (d) HR-STEM image of the top part of the TbMnO$_3$ film. A complicated domain structure is shown by dotted lines marking FE domain walls and pointing up and down polarization vectors.

and contains very narrow (FWHM $\sim 0.2^\circ$) and intense peaks. Finally, the atomic force microscopy (AFM) of h-TMO films [29] reveals a flat and smooth surface morphology with calculated mean-square roughness, $\sim$0.2 nm.

In Fig. 2 we present a high-resolution cross-section TEM image of a h-TMO/YSZ(111) film, showing a coherent epitaxial growth with in-plane epitaxial relationships [−1100]TMO//[1-10]YSZ. The atomically sharp and flat film/substrate interface contains no signs of chemical intermixing and misfit dislocations, pointing out the existence of coherent epitaxy of h-TMO/YSZ(111) films in full agreement with x-ray data (Fig. 1). One can clearly see shifts of Tb ions from the atomic planes, which were also observed for other bulk hexagonal manganites [33–36] and ferrites [37] and argued to be characteristic feature of the "geometric ferroelectricity." Moreover, following the "Tb shifts" along the same atomic layer one can find regions where the characteristic "up"-"up" shift sequence [left part of Fig. 2(b)] changes to the "down"-"down" sequence [right part of Fig. 2(b)]. This signals the crossing of FE domain boundary and allows one to superimpose the TEM image onto the FE domain structure. The latter contains domains with electrical polarization aligned perpendicular to the film plane and with a lateral size varying in the range $\sim$ 5–20 nm. The observed FE domain boundary/wall is very sharp (typically 1 unit cell (u.c.)), directly linking the up- and down-shifted Tb ions. The domains are elongated along the z axis and can originate from the substrate surface as some large domains were seen to form at the atomic steps, originated from the screw dislocations ending at the substrate surface [see Fig. 2(c)]. However, the domain size seems to be not necessarily correlated with the film thickness as shown in Fig. 2(d). It is worth mentioning that according to our TEM study the very first 3–4 u.c. of h-TMO do not reveal pronounced and long-range ordered Tb-shifts, possibly indicating the absence of ferroelectricity in very few layers close to the substrate. Nordlander *et al.* [14] have related the absence of improper ferroelectricity in ultrathin (3-u.c.) YMnO$_3$ films to the mechanical clamping to the substrate, which leads to the vanishing of the long-range order in displacements of Y atoms. Apparently, also in case of our strain-stabilized h-TMO/YSZ films the short-range order Tb displacements can be seen in a selected region close to the substrate in Fig. 2(c) in full agreement with Ref. [14].

Hexagonal structure of TMO films was additionally confirmed by the room-temperature polarization-dependent Raman spectroscopy shown in the inset in Fig. 3(a). Being only visible in the cross-polarization (yx) configuration, the strong Raman line at $\sim 683\,\text{cm}^{-1}$ corresponds nicely to the A_1 mode of the hexagonal structure as shown for hexagonal manganite films [38]. In Fig. 3(a) we present the Raman spectra of the h-TMO film measured at fixed temperatures (the spectra are shifted for clarity) taken by heating and cooling (not shown) the sample in the temperature range $T = 293$–973 K. The Raman spectra in Fig. 3(a) of the film sample were first corrected by the Bose factor, $n + 1 = \frac{1}{1-e^{\hbar\omega/kT}}$, and then normalized to the strongest substrate peak at $\sim 613\,\text{cm}^{-1}$ as can be also seen in the inset in Fig. 3(a). Qualitatively, Fig. 3(a) demonstrates a strong temperature-dependent Raman behavior with suppression of the film A_1 peak, started already from room temperature, and a complete vanishing of the film peak at $T > 873$ K. The subtracted (sample-substrate) Raman spectra presented in Fig. 3(b) allowed us to analyze quantitatively the temperature behavior of a single A_1 film peak by fitting the difference spectra at all measured temperatures by Lorentz lines as shown in Supplemental Material, Fig. SI-2 [29]. One can see in Fig. 3(c) that the intensity, quantified by the area under the A_1 peak and its height, decrease steeply for $T = 300$–450 K and then continuously goes down to zero for $T = 500$–773 K, indicating the existence of a structural phase transition at about 800 K. A similar temperature behavior with vanishing of the A_1 peak for $T > T_C = 1020$ K was reported in h-LuFeO$_3$ film [25]. The position of the A_1 peak in our strain-stabilized h-TMO film shifts almost linearly from $\sim 683\,\text{cm}^{-1}$ at room temperature down to $\sim 668\,\text{cm}^{-1}$ at 773 K [see the inset in Fig. 3(c)]. This linear temperature behavior agrees with that measured in h-YMnO$_3$ bulk samples [24]. Note that the A_1 peak in bulk samples of h-YMnO$_3$ [24]did not vanish for $T > T_C \sim 1000$ K, but rather the symmetry

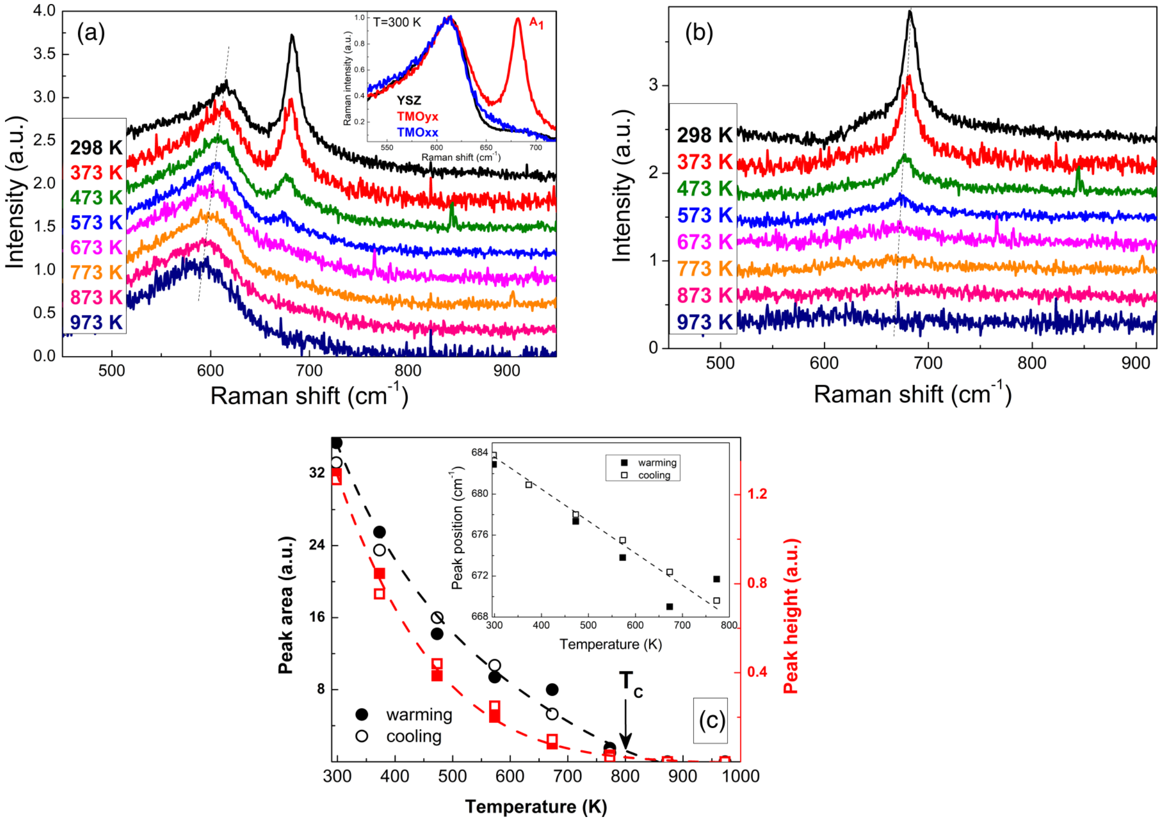

FIG. 3. (a) Unpolarized Raman spectra of a h-TMO/YSZ(111) sample, normalized to the spectrum of the substrate. Inset: room-temperature polarized Raman spectra of a TMO/YSZ(111) film in XX (red) and XY (blue) polarization geometries confirm the hexagonal structure. (b) Evaluated Raman spectra of the h-TMO film. (c) The area (left scale) and the height of the A_1 peak (right scale) by warming (closed symbols) and cooling (open symbols). Phase transition is indicated by peak vanishing at $T_C \sim 800$ K. The inset in (c) shows the peak position as a function of temperature.

changes to A_{1g}. However, for $T > 800$ K we cannot further resolve the Raman peak from our 50-nm-thick h-TMO film because of very small peak intensity, which in addition superimposes with the Raman contribution of the substrate. After cooling down the film to room temperature the intensity and position of the A_1 Raman peak retain to the same level as before heating, indicating no sizable strain relaxation effects in this film. Thus, the temperature-dependent Raman study indicates that a reversible structural phase transition into a paraelectric $P6_3/mmc$ structure occurs around $T_C \sim 800$ K in the optimally grown h-TMO/YSZ(111) film.

To support our Raman data and to get an additional insight into the structural phase transition in hexagonal h-TMO films we studied the temperature-dependent optical ellipsometry for $T = 300$–1200 K. In Fig. 4(a) the time dependences of the ellipsometric phase shift, $\Delta(T)$, and polarization rotation, $\Psi(T)$, angles are shown during the cooling down of the film. Using double-side polished YSZ substrate we were able to monitor the oscillations in $\Delta(T)$ and $\Psi(T)$ due to the interference of the laser beam, reflected from the top and bottom surface of the plane parallel substrate, the thickness of which was changing due to thermal expansion. This allows us to measure the temperature of the sample by calculating the number of oscillations and calibrating the temperature by using a pyrometer: namely, $T = 1200$ K was achieved at the highest current $I = 28$ A. One can see in Fig. 4(a) that both $\Delta(T)$ and $\Psi(T)$ show the following characteristic features: (a) continuous changes by about 3°–5° at the beginning and at the end of the time scan; and (2) a steplike change of the signal, especially pronounced in $\Delta(T)$, changing by 10°, in the middle part of the scan. In Fig. 4(b) the timescale was recalculated into the temperature scale by using the relation $T(t) = 293\,\text{K} + 18\,\text{K} \times t$, where the initial point of the x scale at $t = 0$ corresponds to the finally achieved room temperature $T = 293$ K (20 °C). Apparently, both ellipsometric angles $\Delta(T)$ and $\Psi(T)$ change drastically for $T = 600$–800 K, indicating the phase transition takes place within the same temperature interval as was observed in Raman spectroscopy (see Fig. 3). In addition, the temperature dependence of the real part of the refractive index, $N(T)$ [right scale in Fig. 4(b)], was evaluated by assuming a simple optical model [29] of a homogeneous film grown on YSZ substrate with $N_{\text{YSZ}} = 2.15$ at $\lambda = 632.8$ nm (see Ref. [39]). At room temperature the evaluated refractive index for a h-TMO film, $n \sim 2.12$, fits nicely to the values measured for YMnO_3 (Ref. [40]). It decreases drastically from $n = 2.12$ to $n = 2.0$, i.e., by 6%, when the film undergoes the FE/PE phase transition. The endpoint of this transition in $N(T)$ curve can be assigned to the Curie temperature, $T_C = 800$ K, in good agreement with the vanishing of the A_1 Raman peak

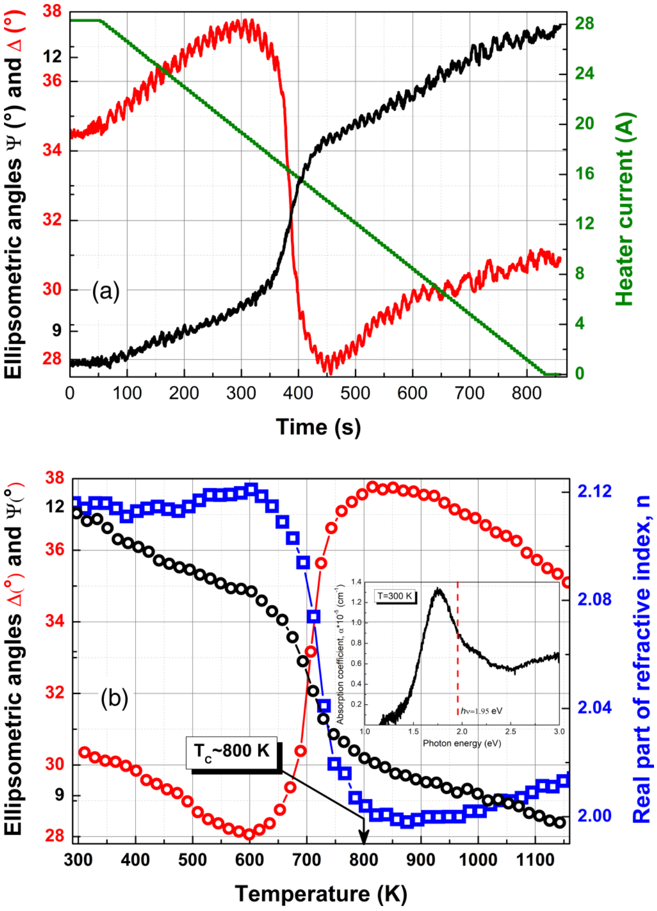

FIG. 4. Time- (a) and temperature (b) dependences of ellipsometric phase shift, Δ, and polarization rotation, Ψ, angles as well as of the calculated refractive index, *n*. A distinct steplike decrease of *n* by 6% indicates the phase transition, the end point of which marks $T_C \sim 800$ K. The inset in (b) shows the absorption spectrum of h-TMO/YSZ(111) film measured at room temperature.

in Fig. 3(c). With thermal expansion coefficient $\sim 10^{-5}$/K and within the temperature change $\sim 10^3$ K, the estimated change of the film thickness $d = 50$ nm at room temperature by heating/cooling is 0.5 nm, i.e. ~1 u.c. Such small thickness changes cannot result in the observed thermal ellipsometry behavior (see Fig. 4). The origin of the observed ellipsometric behavior should be related to the change of optical properties and electronic structure of h-TMO at the structural phase transition. The photon energy $E \sim 1.96$ eV of the He-Ne laser radiation falls within a strong and narrow absorption band with the center at $E = 1.75$ eV, as demonstrated by the measured absorption spectrum for a h-$TbMnO_3$/YSZ(111) film in the inset of Fig. 4(b) (see also Refs. [41]). According to the theory [42], the origin of this absorption band in h-manganites is the interband charge-transfer transition from the occupied oxygen O2*p* states into the empty Mn3*d* states. Hence, we can conclude that at the structural phase transition the *p*-*d* charge transfer changes significantly in the h-TMO film. Here we can speculate that a modification of the electronic band structure during the $P6_3/mmc$ (PE) to $P6_3cm$ (FE) structural phase transition influences a charge transfer from the O2*p* to Mn3*d* states. Note that charge transfer from the Y-O_T (apical oxygen) bonds to the O_T-Mn bonds of Mn3*d*-O2*p* hybridized states was found to be responsible for the enhanced ferroelectricity during the annealing-induced orthorhombic-hexagonal phase transition in bulk $YMnO_3$ (Ref. [43]). However, by doing monochromatic ellipsometry we cannot measure the changes of spectral weight transfer at the phase transition. In addition, the absorption peak is known to show a "blue" shift by decreasing temperature, $T = 300$–15 K [41].

Concluding this part, one can say that h-TMO films were epitaxially grown by MAD in a strain-stabilized state on YSZ(111) substrate. The estimated in- and out-of-plane tensile stress at room temperature are −1.2 and -3%, respectively. Importantly, according to measurements of Raman spectroscopy and optical ellipsometry, the h-TMO films prepared in such a way demonstrate a reversible structural phase transformation with $T_C \sim 800$ K. We call this *intrinsic* behavior as it is related to the h-TMO material, prepared in the form of strain-stabilized film.

In addition, we would like to shed light on the two *extrinsic* effects manifesting themselves as irreversible or partially reversible phase transformations observed in: (1) the stoichiometric film sample with constrained geometry; and (2) the nonstoichiometric h-TMO film with ∼ 5–10% of Tb excess (molar ratio Tb/Mn = 1.2). In both cases the temperature-induced stress relaxation in the film samples plays a dominant role in the irreversible phase transformation.

Firstly, in Fig. 5 we present the *in situ* TEM heating experiments, performed to monitor the changes of atomic structure and morphology of ferroelectric domains in the stoichiometric h-TMO lamella sample with increasing temperature. Electron diffraction patterns, collected at every 5 K by heating, do not show any changes for $T = 300$–400 K. However, already at $T = 405$ K new superstructure spots, marked with the white arrow in the inset in Fig. 5(c), show up, signaling the beginning of a phase transformation. Finally, at $T = 410$ K all spots originating from the ferroelectric hexagonal $P6_3cm$ structure along with Tb shifts disappear and another hexagonal $P6_3/mmc$ structure is formed similar to the structural transformation described for the bulk h-$YMnO_3$ [44]. One has to note that such structural transformation was found to be irreversible in the h-TMO film lamella. Most probably, it is related to the temperature-induced full stress relaxation because of a plastic deformation of very thin (∼ 20 nm) TEM lamella with very large aspect ratio 1 × 10. A direct evidence of stress relaxation by formation of misfit dislocations in the TEM lamella sample can be seen in Fig. 5, which shows the high-resolution transmission electron microscopy (HRTEM) images collected before (e) and after (f) the *in situ* TEM annealing. One can see that the sample, being initially coherently strained and displaying FE domains, was fully relaxed and domain-free after the thermal cycling (300-410-300 K), which results in the formation of a system of misfit dislocations placed at a distance ∼ 2 nm. Considering the above estimated in-plane tensile stress as a lattice misfit $f = 1.2\%$, the calculated equilibrium distance between dislocations $d = a_{\mathrm{YSZ}}/(2f) = 2.1$ nm is in excellent agreement with observations in Fig. 5(f). The relaxation of stress presumably by means of plastic deformation in the TEM lamella drives the formation of a hexagonal paraelectric phase already at $410\ \mathrm{K} \ll T_C \sim 800$ K. Considering a specially prepared TEM

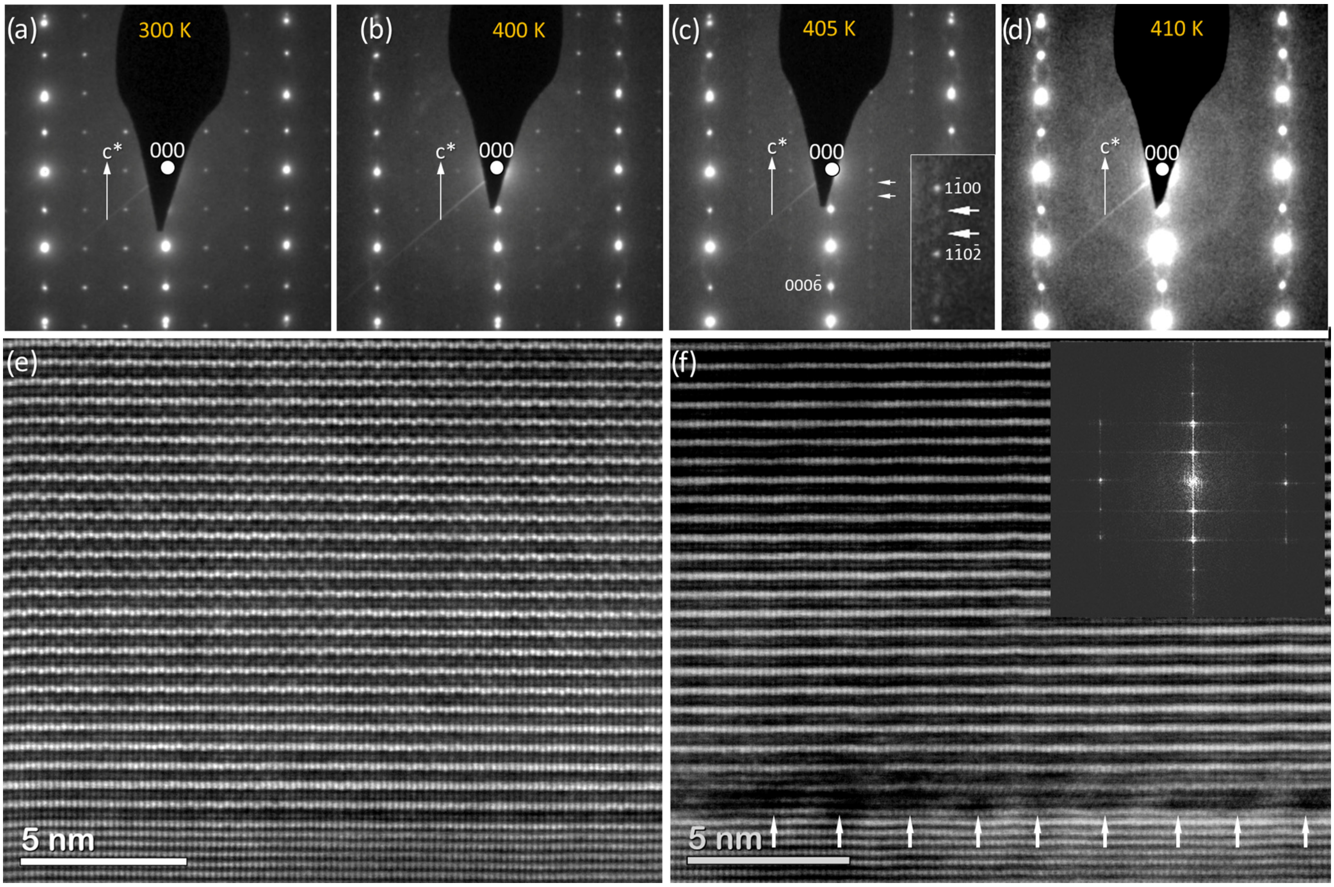

FIG. 5. (a)–(d) Electron diffraction, collected at different temperatures upon heating of the TEM lamella up to 410 K. (e), (f) high-resolution STEM images. The initial hexagonal ($P6_3cm$) structure with Tb shift (e) was irreversibly transformed into a hexagonal ($P6_3/mmc$) structure with planar Tb planes (f). This irreversible phase transformation is caused by strain relaxation actuated by formation of a system of misfit dislocations as evidenced in (f).

sample the observed reduction of T_C as well as the irreversible character of phase transition both point out its extrinsic origin.

Secondly, a partially reversible phase transition, accompanied by a strong reduction of the Raman intensity after temperature cycling (300-1000-300 K), was observed in the nonstoichiometric h-TMO films with precursor molar ratio Tb/Mn = 1.2. XRD patterns in Fig. 6(b) indicate a strain relaxation in the film as the c-lattice parameter decreases from $c = 1.118$ nm in the as-prepared state, down to $c = 1.112$ nm after Raman annealing. Note that this difference $\Delta c \sim 0.006$ nm is very close to the difference between the c axis of the FE ($P6_3cm$) and PE ($P6_3/mmc$) structures of $YMnO_3$ [45]. An additional heating/annealing to 900 °C/15 min and quenching the film from the deposition temperature down to 600 °C results in the coexistence of two crystallographic hexagonal domains with different out-of-plane lattice parameters, 1.118 and 1.114 nm, pointing out the coexistence of ferroelectric and paraelectric phases in the film. Note that the c-lattice constant of the stoichiometric h-TMO film did not change after the Raman annealing [see Fig. 6(a)]. To correlate the global (XRD) strain relaxation behavior [Fig. 6(b)] with atomic-scale changes of the h-TMO microstructure induced by heating, the cross-section TEM specimens were cut from a stoichiometric film with reversible (R) behavior and from a nonstoichiometric film with irreversible (IR) behavior after performing the "Raman" annealing and second quench. The high-resolution STEM HAADF images, shown in Figs. 6(c)–6(f), were collected using identical parameters of the electron microscope for both films. The original images were filtered with Fast Fourier Transform (FFT) using selected space frequencies and their contrast was enhanced [see insets in Figs. 6(c) and 6(d)]. Apparently, the R film displays a homogeneous microstructure with FE domains having a lateral size of more than 30 nm [Fig. 6(e)]. The filtered image of the IR film [Fig. 6(f)] demonstrates an inhomogeneous microstructure with FE domains, intermixed by PE domains (flat Tb planes) with ∼3–7-nm size. [Moreover, the interface layer with PE structure is by $\sim 50\%$ thicker in the IR film [Fig. 6(d)] as compared to that in the R film [Fig. 6(c)]. The observation of inhomogeneous microstructure of the IR film with coexisting FE and PE domains correlates nicely with the XRD pattern in Fig. 6(b).

Thus, there can be three scenarios of the strain-driven structure/ferroelectricity relationship in the prepared h-TMO/YSZ(111) films: (1) reversible structural phase transition at $T_C \sim 800$ K in stoichiometric films; their thermal behavior is strongly influenced by reversible strain changes;

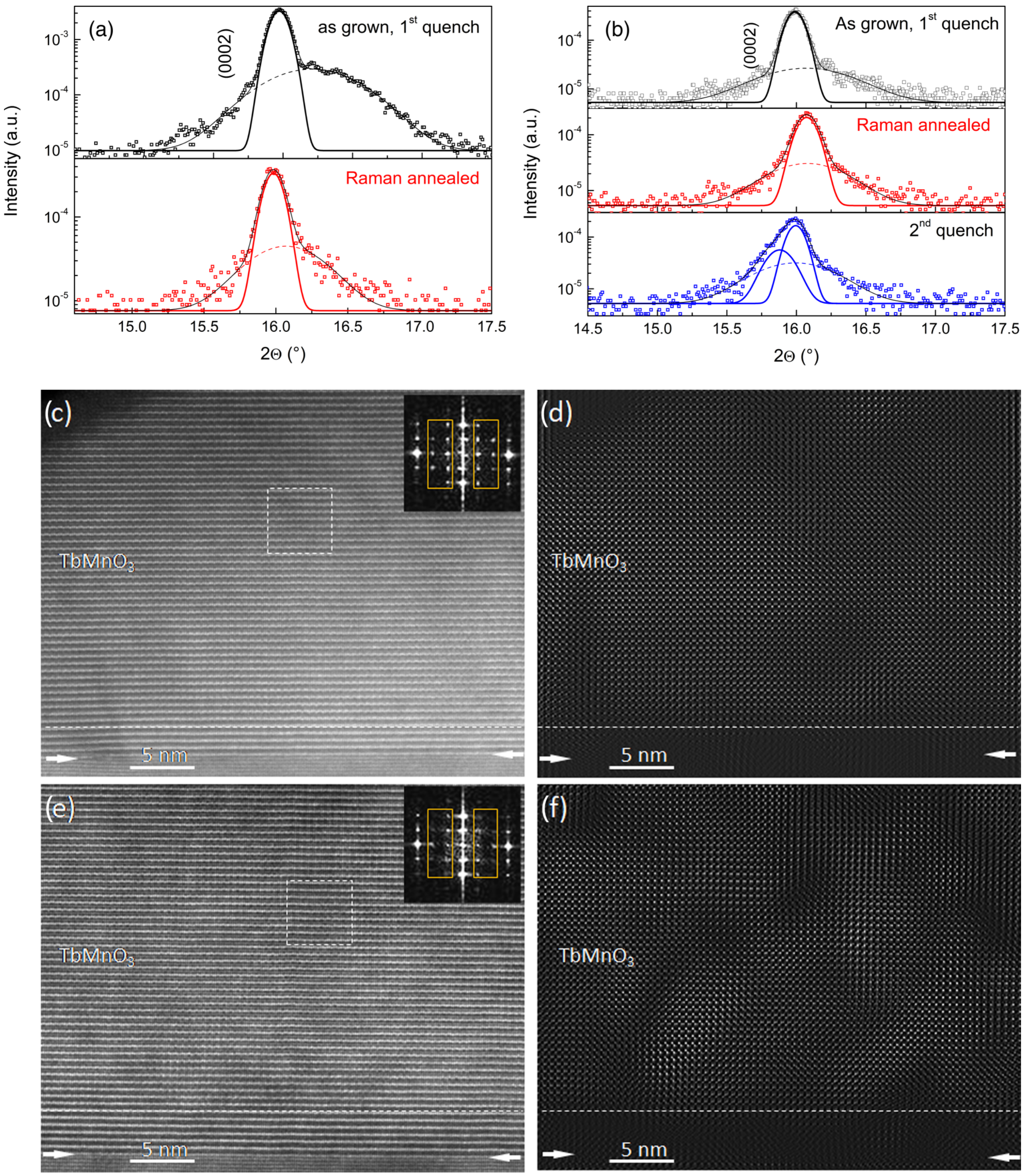

FIG. 6. XRD patterns (a), (b), and original (c), (d) and filtered (e), (f) HRSTEM images of the two $TbMnO_3$ films, showing the reversible (a), (c), (e) and irreversible (b), (d), (f) behavior after temperature-dependent Raman measurements. Insets in (b) and (c) show two FFT patterns from the selected areas marked with the white line. The spots inside the selected areas in the FFTs (orange contours) were used for the filtering to reveal the distribution of PE and FE phases. The FE phase demonstrates sharper and brighter spots because of pronounced up and down shifts of Tb ions, while the PE phase demonstrates almost flat Tb planes. XRD patterns close to the (0002) peak of the h-TMO for film with reversible (a) thermal behavior shows almost no changes in the *c*-lattice parameter whereas the film with irreversible (b) behavior demonstrates distinct changes related to the coexistence of FE and PE phases.

(2) partially reversible phase transition at 800 K in the nonstoichiometric film with Tb excess, accompanied by a partial strain relaxation and formation of two coexisting phases, i.e., FE $P6_3cm$ and PE $P6_3/mmc$, and (3) irreversible phase transition at 410 K due to full strain relaxation and formation of misfit dislocations in the stoichiometric film, prepared as TEM lamella sample with strongly reduced dimensions and large aspect ratio. Note that in all cases the phase transformation occurs from the low-temperature FE $P6_3cm$ structure to the high-temperature PE $P6_3/mmc$ structure and no signs of the orthorhombic phase, inherent to bulk $TbMnO_3$ material were found.

Probably, a hint for the understanding of thermal behavior in h-TMO films is given by Nordlander *et al.* [14], as they related the suppression of the improper ferroelectricity close to the interface in the strain-free $YMnO_3$/YSZ(111) to mechanical clamping to the substrate. Our as-grown and coherently strained h-TMO films also show the same phenomenology (see Fig. 2), i.e., almost the whole 50-nm-thick stoichiometric h-TMO film shows FE $P6_3cm$ structure, whereas the first 3 u.c., being clamped to the substrate, reside in the PE $P6_3/mmc$ structure. This coherently strained and almost defect-free film shows reversible and strong temperature- and strain-induced changes in the A_1 Raman peak intensity for $T = 300$–1000 K [see Fig. 3(c)]. It is natural to assume that thermal behavior of the nonstoichiometric h-TMO films with 5–7% of Tb excess can be influenced by defects. Being viewed as internal interfaces, they suppress the FE phase by pinning the film to the defect and lead to a suppressed mobility of FE/structural domains and, hence, to changes in the out-of-plane stress detected by XRD [Fig. 6(b)]. An additional high-temperature annealing of the IR film, accompanied by temperature/strain-induced changes of the film microstructure (Fig. 6), leads to the redistribution and/or healing of defects and may result in partial restoring of the FE phase. An additional support for such scenario can be seen in the AFM images in Fig. S-1, which show pronounced changes of the film morphology in the IR film and almost no morphological changes in the R film after Raman annealing.

In conclusion, high-quality epitaxial thin films of hexagonal $TbMnO_3$ were grown on YSZ(111) substrates by using MAD technique in an oxygen-rich atmosphere. Compared to the previously reported PLD-grown films they display a perfect crystallinity and atomically sharp film/substrate interfaces. Ferroelectric domains, originated from the shift of Tb ions from the atomic plane, with sharp domain boundaries were visualized by means of high-resolution STEM. Structural phase transition at $T_C \sim 800$ K was determined by the temperature-dependent Raman spectroscopy and optical ellipsometry. Ferroelectric/structural domains in epitaxially stabilized h-TMO films depend drastically on the macroscopic stress state of the film influenced by temperature and film stoichiometry.

ACKNOWLEDGMENTS

R.M. acknowledges financial support from Erasmus Plus programme, European Union, Georg-August-Universität Göttingen and IISER Pune. V.R., U.R., S.M., and V.M. acknowledge financial support from Deutsche Forschungsgemeinschaft via SFB 1073 (TP A02, Z02). Authors thank M. D. Bongers for XRD phi-scan measurements. The use of equipment in the “Collaborative Laboratory and User Facility for Electron Microscopy” (CLUE) www.clue.physik.uni-goettingen.de is gratefully acknowledged.

---

[1] B. Lorenz, ISRN Condens. Matter Phys. **2013**, 497073 (2013).
[2] M. Balli, B. Roberge, P. Fournier, and S. Jandl, Crystals **7**, 44 (2017).
[3] N. Lee, Y. J. Choi, M. Ramazanoglu, W. Ratcliff, V. Kiryukhin, and S. W. Cheong, Phys. Rev. B **84**, 020101(R) (2011).
[4] X. Li, C. Lu, J. Dai, S. Dong, Y. Chen, N. Hu, G. Wu, M. Liu, Z. Yan, and J. M. Liu, Sci. Rep. **4**, 7019 (2015).
[5] M. Lilienblum, T. Lottermoser, S. Manz, S. M. Selbach, A. Cano, and M. Fiebig, Nat. Phys. **11**, 1070 (2015).
[6] D. Lee, A. Yoon, S. Y. Jang, J. G. Yoon, J. S. Chung, M. Kim, J. F. Scott, and T. W. Noh, Phys. Rev. Lett. **107**, 057602 (2011).
[7] B. B. Van Aken, T. T. M. Palstra, A. Filippetti, and N. Spaldin, Nat. Mater. **3**, 164 (2004).
[8] C. J. Fennie and K. M. Rabe, Phys. Rev. B **72**, 100103(R) (2005).
[9] A. N. Pirogov, Acta Crystallogr. Sect. B **72**, 1 (2016).
[10] J. A. Mundy, C. M. Brooks, M. E. Holtz, J. A. Moyer, H. Das, A. F. Rebola, J. T. Hero, J. D. Clarkson, S. M. Disseler, and Z. Liu *et al.*., Nature (London) **537**, 523 (2016).
[11] L. W. Martín, Y. H. Chu, and R. Ramesh, Mater. Sci. Eng.: R: Reports **68**, 89 (2010).
[12] S. Y. Jang, D. Lee, J.-H. Lee, T. W. Noh, Y. Jo, M.-H. Jung, and J.-S. Chung, Appl. Phys. Lett. **93**, 162507 (2008).
[13] J. H. Lee, P. Murugavel, D. Lee, and T. W. Noh, Appl. Phys. Lett. **90**, 012903 (2007).
[14] J. Nordlander, M. Campanini, M. D. Rossell, R. Erni, Q. N. Meier, A. Cano, N. A. Spaldin, M. Fiebig, and M. Trassin, Nat. Commun. **10**, 5591 (2019).
[15] J. Fontcuberta, C. R. Phys. **16**, 204 (2015).
[16] T. Kordel, C. Wehrenfennig, D. Meier, Th. Lottermoser, M. Fiebig, I. Gélard, C. Dubourdieu, J.-W. Kim, L. Schultz, and K. Dörr, Phys. Rev. B **80**, 045409 (2009).
[17] J. H. Lee, P. Murugavel, H. Ryu, D. Lee, J. Y. Jo, J. W. Kim, H. J. Kim, K. H. Kim, Y. Jo, M. H. Jung, Y. H. Oh, Y. W. Kim, J. G. Yoon, J. S. Chung, and T. W. Noh, Adv. Mater. **18**, 3125 (2006).
[18] J. H. Lee, D. Lee, T. W. Noh, P. Murugavel, J. W. Kim, K. H. Kim, Y. Jo, M. H. Jung, J. G. Yoon, and J. S. Chung, J. Mater. Res. **22**, 2156 (2007).
[19] D. J. Kim, T. R. Paudel, H. Lu, J. D. Burton, J. G. Connell, E. Y. Tsymbal, S. S. A. Seo, and A. Gruverman, Adv. Mater. **26**, 7660 (2014).
[20] H. Sim, J. Jeong, H. Kim, S. W. Cheong, and J. G. Park, J. Phys.: Condens. Matter **30**, 105601 (2018).
[21] M. Fiebig, V. V. Pavlov, and R. V. Pisarev, J. Opt. Soc. Am. B **22**, 96 (2005).
[22] S. A. Denev, T. T. A. Lummen, E. Barnes, A. Kumar, and V. Gopalan, J. Am. Ceram. Soc. **94**, 2699 (2011).
[23] T. Iizuka-Sakano, E. Hanamura, and Y. Tanabe, J. Phys.: Condens. Matter **13**, 3031 (2001).
[24] H. Fukumura, S. Matsui, H. Harima, K. Kisoda, T. Takahashi, T. Yoshimura, and N. Fujimura, J. Phys.: Condens. Matter **19**, 365239 (2007).
[25] S. M. Disseler, J. A. Borchers, C. M. Brooks, J. A. Mundy, J. A. Moyer, D. A. Hillsberry, E. T. Thies, D. A. Tenne, J. Heron, and M. E. Holtz, Phys. Rev. Lett. **114**, 217602 (2015).

[26] C. Dubourdieu, G. Huot, I. Gelard, H. Roussel, O. I. Lebedev, and G. Van Tendeloo, Philos. Mag. Lett. **87**, 203 (2007).

[27] M. Jungbauer, S. Hühn, R. Egoavil, H. Tan, J. Verbeeck, G. Van Tendeloo, and V. Moshnyaga, Appl. Phys. Lett. **105**, 251603 (2014).

[28] H. Fujiwara, *Spectroscopic Ellipsometry. Principles and Applications* (John Wiley & Sons, Ltd., Chichester, UK, 2007).

[29] See Supplemental Material at http://link.aps.org/supplemental/10.1103/PhysRevB.102.104106 for AFM images of the films, fitting of Raman peaks and calculation of the refractive index.

[30] K. H. Wu, H.-J. Chen, C. C. Hsieh, C. W. Luo, T. M. Uen, J.-Y. Lin, and J. Y. Juang, J. Supercond. Novel Magn. **26**, 801 (2013).

[31] N. Jehanathan, O. I. Lebedev, I. Gélard, C. Dubourdieu, and G. Van Tendeloo, Nanotechnology **21**, 075705 (2010).

[32] https://crystal-gmbh.com/shared/downloads/datenblaetter/substrates_de/ZrO2_Y_YSZ_Zirconium_Oxide.pdf.

[33] M. G. Han, Y. Zhu, L. Wu, T. Aoki, V. Volkov, X. Wang, S. C. Chae, Y. S. Oh, and S. W. Cheong, Adv. Mater. **25**, 2415 (2013).

[34] Q. H. Zhang, L. J. Wang, X. K. Wei, R. C. Yu, L. Gu, A. Hirata, M. W. Chen, C. Q. Jin, Y. Yao, Y. G. Wang, and X. F. Duan, Phys. Rev. B **85**, 020102(R) (2012).

[35] T. Matsumoto, R. Ishikawa, T. Tohei, H. Kimura, Q. Yao, H. Zhao, X. Wang, D. Chen, Z. Cheng, N. Shibata, and Y. Ikuhara, Nano Lett. **13**, 4594 (2013).

[36] Q. Zhang, G. Tan, L. Gu, Y. Yao, C. Jin, Y. Wang, X. Duan, and R. Yu, Sci. Rep. **3**, 1 (2013).

[37] V. V Roddatis, A. R. Akbashev, S. Lopatin, and A. R. Kaul, Appl. Phys. Lett. **103**, 112907 (2013).

[38] N. T. M. Hien, S. Y. Oh, X. B. Chen, D. Lee, S. Y. Jang, T. W. Noh, and I. S. Yang, J. Raman Spectrosc. **42**, 1774 (2011).

[39] D. L. Wood and K. Nassau, Appl. Opt. **21**, 2978 (1982).

[40] L. G. Vieira, J. L. Ribeiro, O. Santo, and P. B. Tavares, J. Optics **14**, 045707 (2012).

[41] W. S. Choi, S. J. Moon, S. S. A. Seo, D. Lee, J. H. Lee, P. Murugavel, T. W. Noh, and Y. S., and Lee, Phys. Rev. B **78**, 054440 (2008).

[42] A. S. Moskvin and R. V. Pisarev, Low Temp. Phys. **36**, 489 (2010).

[43] S.-H. Liu, J.-C.-A. Huang, X. Qi, W.-J. Lin, Y.-J. Siao, C.-R. Lin, J.-M. Chen, M.-T. Tang, Y.-H. Lee, and J.-C. Lee, AIP Adv. **1**, 032173 (2011).

[44] S. C. Abrahams, Acta Crystallogr. B **65**, 450 (2009).

[45] A. S. Gibbs, K. S. Knight, and Ph. Lightfoot, Phys. Rev. B **83**, 094111 (2011).